

To make the device accessible and measurable by a vector network analyzer (VNA), transitions between SIW and a standard SMA connector were added at every port. The transition is the same for all ports and can be either a SIW-microstrip-SMA junction or a direct SIW-SMA one. The former can be designed by following the guidelines shown in [12] while the latter, which is the implemented solution, can be designed following the procedure presented in [13]. To space SMA connectors sufficiently to accommodate the VNA cables, optimally mitered 90° curves were also added on four ports. It is worth noting that the inclusion of the transitions to coaxial cables and mitered curves does not change the phase relationships among the output signal given that the double symmetry is maintained.

The final coupler is shown in Figure 2. The size of the board is $90 \times 70 \text{ mm}^2$, while the core of the circuit shown in Figure 1 is only $40 \times 32 \text{ mm}^2$. Diameter of the vias is 0.6 mm, whereas the spacing among them is in the range 1.0–1.3 mm, depending on the length of the waveguide to be realized. This spacing is sufficient to avoid energy leakage through lateral walls.

The simulated scattering parameters are shown in Figures 3 and [4]. Return loss and isolation are higher than 15 dB in the band 11.0–12.4 GHz and higher than 20 dB in the band 11.2–12.3 GHz. The transmission coefficients are well balanced, within 1 dB variation in the band 10.7–12.3 GHz. The resonance at high frequency deteriorates the response above 12.5 GHz. However, it is above the band of interest for the application the coupler was designed.

3. EXPERIMENTAL RESULTS

A prototype was built (Fig. 5) and measured using an Agilent 8510C VNA.

Experimental results are in good agreement with simulations, as shown in Figures 6 and [7]. Most of the degradation of the return loss can be imputed to connectors. The resonance at 12.85 GHz is confirmed by measurements.

The measured phase difference $\phi_{14} - \phi_{16}$ (Fig. 8) satisfies the Eq. (3) with a deviation of $+5^\circ / -8^\circ$ in the band where the return loss is 13 dB. Figure 9 shows the phase balance of the transmission coefficients of the prototype built. This single graph shows the phase differences $\phi_{24} - \phi_{15}$, $\phi_{26} - \phi_{15}$, $\phi_{35} - \phi_{15}$ (curves with triangles, X and asterisks, respectively), the phase difference $\phi_{36} - \phi_{14}$ (curve with diamonds), and finally the phase difference $\phi_{34} - \phi_{16}$ (curve with squares). All these quantities should be ideally zero. As can be seen there are variable results, from a minimum of 3° to a maximum of 10° of phase unbalance. The spike at 12.85 GHz is due to the resonance.

Finally, the measured total insertion loss, computed as $10 \cdot \log_{10}(P_{\text{in}}/P_{\text{out}})$, is close to 0.75–0.8 dB in the band of interest, as shown in Figure 10.

4. CONCLUSION

A compact six-port directional coupler made in SIW technology has been designed and experimentally characterized. The input power is equally divided into three output ports while other two ports are isolated. The final device has been assembled and measured. Experimental results show good agreement with simulations. The device can be used stand-alone or inside more complex circuits, by removing the SIW-SMA transitions. Its performance promises a number of actual applications.

ACKNOWLEDGMENT

The prototype shown in this work was built by Somacis SpA.

REFERENCES

1. X. Xu, R.G. Bosisio, and K. Wu, A new six-port junction based on substrate integrated waveguide technology, *IEEE Trans Microwave Theory Tech* 53 (2005), 2267–2273.
2. T. Djerafi, M. Daigle, H. Boutayeb, X. Zhang, and K. Wu, Substrate integrated waveguide six-port broadband front-end circuit for millimeter-wave radio and radar systems, In: *Proceedings of the 39th European Microwave Conference (EuMA)*, Rome, Italy, 2009, pp. 77–80.
3. A. Doghri, T. Djerafi, A. Ghiotto, and K. Wu, Broadband substrate-integrated-waveguide six-port applied to the development of polarimetric imaging radiometer, In: *Proceedings of the 41st European Microwave Conference, EuMA*, Manchester, UK, 2011, pp. 393–396.
4. M. Dusek and J. Sebesta, Design of substrate integrated waveguide six-port for 3.2 GHz modulator, In: *34th International Conference on Telecommunications Signal Processing (TSP)*, Budapest, Hungary, 2011, pp. 274–278.
5. W. Li-nan, Z. Xu-chun, T. Chuang-ming, and Z. Ming, A new substrate integrated waveguide six-port circuit, In: *IEEE International Conference on Microwave and Millimeter Wave Technology (ICMMT)*, Chengdu, China, 2010, pp. 59–61.
6. J.X. Chen, W. Hong, H.J. Tang, P.P. Yan, B. Liu, and K. Wu, A millimeter wave six-port network using half-mode substrate integrated waveguide, *J Infrared Millim Terahertz Waves* 33 (2012), 348–356.
7. J.M. Rebollar, J. Esteban, and C. Blance, Computer aided design of non-symmetric six-port branch-waveguide directional couplers, In: *Proceedings of the 20th European Microwave Conference*, Budapest, 1990, pp. 1041–1046.
8. E. Kuhn, H. Schmiedel, and R. Waugh, Six-port branch-waveguide directional couplers, In: *Proceedings of the 16th European Microwave Conference*, Dublin, 1986, pp. 453–458.
9. P. Carle, Optimised design of eight-port branch-waveguide directional couplers, In: *IEEE MTT-S International Microwave Symposium Digest*, Boston, MA, 1991, pp. 853–856.
10. F. Alessandri, M. Giordano, M. Guglielmi, G. Martirano, and F. Vitulli, A new multiple-tuned six-port riblet-type directional coupler in rectangular waveguide, *IEEE Trans Microwave Theory Tech* 51 (2003), 1441–1448.
11. Y. Cassivi, L. Perreggini, P. Arcioni, M. Bressan, K. Wu, and G. Conciauro, Dispersion characteristics of substrate integrated rectangular waveguide, *IEEE Microwave Wireless Compon Lett* 12 (2002), 333–335.
12. D. Deslandes, Design equations for tapered microstrip-to-substrate integrated waveguide transitions, In: *IEEE MTT-S International Microwave Symposium Digest*, Anaheim, CA, 2010, pp. 23–28.
13. A. Morini, M. Farina, C. Cellini, T. Rozzi, and G. Venanzoni, Design of low-cost non-radiative SMA-SIW launchers, In: *IEEE Proceedings of the 36th European Microwave Conference*, Manchester, 2006, pp. 526–529.

© 2015 Wiley Periodicals, Inc.

HYBRID DUAL-ANTENNA FOR THE 3.6-GHz LTE OPERATION IN THE TABLET COMPUTER

Kin-Lu Wong and Hsuan-Jui Chang

Department of Electrical Engineering, National Sun Yat-Sen University, 80424 Kaohsiung, Taiwan; Corresponding author: wongkl@ema.ee.nsysu.edu.tw

Received 30 March 2015

ABSTRACT: A hybrid dual-antenna formed by an inverted-F antenna (IFA) and an open-slot antenna (OSA) for the 3.6-GHz LTE operation

(3.4–3.8 GHz) in the tablet computer is presented. The dual-antenna is printed on a 0.8-mm thick FR4 substrate and has a compact planar structure of $4 \times 30 \text{ mm}^2$. The dual-antenna comprises a clearance region wherein the IFA is disposed and a metal pad wherein the OSA is embedded. The IFA's shorting strip is grounded through the metal pad to the device ground plane, so that an integrated compact dual-antenna structure is obtained. As the IFA and OSA have different excitation mechanisms (electric-current excitation on the IFA vs. magnetic-current excitation on the OSA), the two antennas are expected to have different near-field characteristics, thereby leading to decreased coupling. The proposed dual-antenna has a measured isolation of better than about 12 dB over the operating band. The IFA and OSA have measured antenna efficiencies of about 72%–86% and 57%–78%, respectively. Good envelope correlation coefficient of less than 0.1 is obtained. Over the operating band, the ergodic capacity of the dual-antenna is calculated to be about 9.8–10.6 bps/Hz. Details of the proposed dual-antenna are presented. © 2015 Wiley Periodicals, Inc. *Microwave Opt Technol Lett* 55:2592–2598, 2015; View this article online at wileyonlinelibrary.com. DOI 10.1002/mop.29387

Key words: mobile antennas; dual-antenna; hybrid antennas; tablet computer antennas; LTE antennas; small-size antennas

1. INTRODUCTION

The dual-antenna formed by integrating two similar or same antennas into a compact configuration [1–6] is attractive for the diversity or MIMO (multiinput multioutput) operation in the mobile communication device. To achieve compact configuration with a small size for mobile device applications, the two antennas are generally spaced very close to each other. In this case, the technique of using a neutralization line (NL) [1–3] or multiple NLs [4,5] or an inductor-loaded NL [6] connected between the two antennas has been shown to be useful to achieve acceptable isolation for the dual-antenna. However, the design process for selecting proper dimensions of the NL such as its width and length is usually tedious. This makes it inconvenient in achieving a compact dual-antenna structure for practical applications.

Other techniques for enhancing the isolation of two closely spaced antennas have also been reported. The techniques include

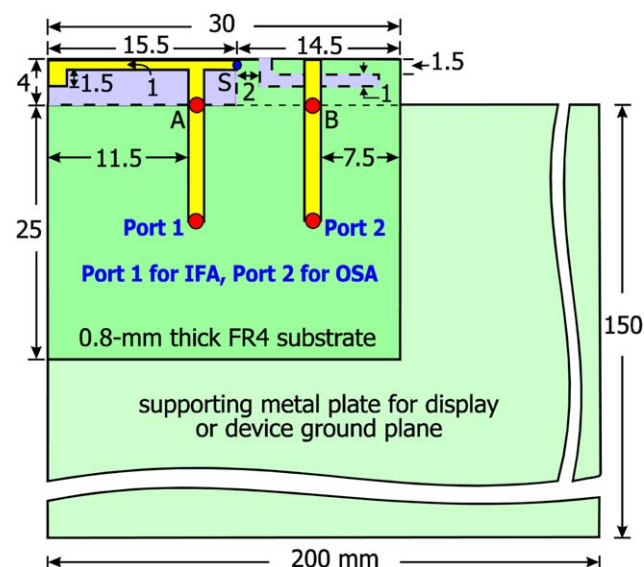


Figure 1 Geometry of the proposed hybrid dual-antenna formed by an IFA and an open slot antenna (OSA) for the 3.6-GHz LTE operation in the tablet computer. [Color figure can be viewed in the online issue, which is available at wileyonlinelibrary.com]

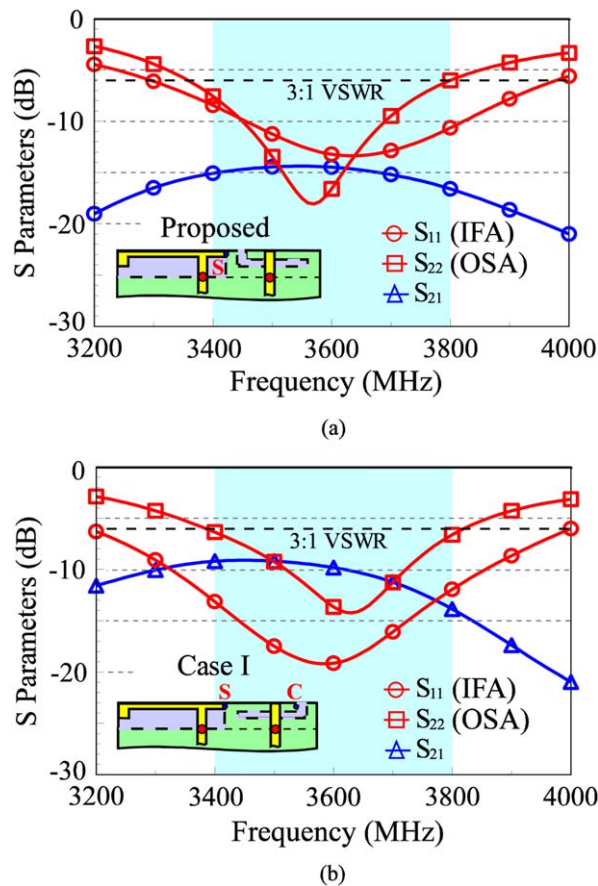


Figure 2 Simulated S parameters of (a) the proposed design (open slot therein extending away from the IFA) and (b) the case with the open slot therein extending toward the IFA (Case I). [Color figure can be viewed in the online issue, which is available at wileyonlinelibrary.com]

disposing a protruded ground pad between two antennas [7–9], or placing quarter-wavelength strip resonators in the clearance region between two antennas [10–12], or embedding a quarter-wavelength slot resonator in the device ground plane between two antennas [13,14], and so forth. In these cases, the two antennas are not connected to each other, which are different from the dual-antenna connected with the NL [1–6] to achieve an integrated and compact structure.

In this article, we propose a hybrid dual-antenna formed by an inverted-F antenna (IFA) and an open-slot antenna (OSA). The application of the proposed dual-antenna for the 3.6-GHz LTE operation (3.4–3.8 GHz band) [15,16] in the tablet computer is studied. The IFA and OSA are integrated to achieve a compact structure by connecting the IFA's shorting strip to the metal pad wherein the OSA is embedded. In this case, the dual-antenna has a low profile of 4 mm and can be disposed on a thin dielectric substrate of $4 \times 30 \text{ mm}^2$. As the IFA and OSA are excited based on different excitation mechanisms (electric-current excitation for the IFA and magnetic-current excitation for the OSA), it is expected that the isolation of the dual-antenna can be decreased. The measured results in this study show that the hybrid dual-antenna has an isolation of better than about 12 dB over the operating band between the IFA and OSA. The simulated results also indicate that the isolation of the proposed dual-antenna is better than that of the cases with two same IFAs or two same OSAs.

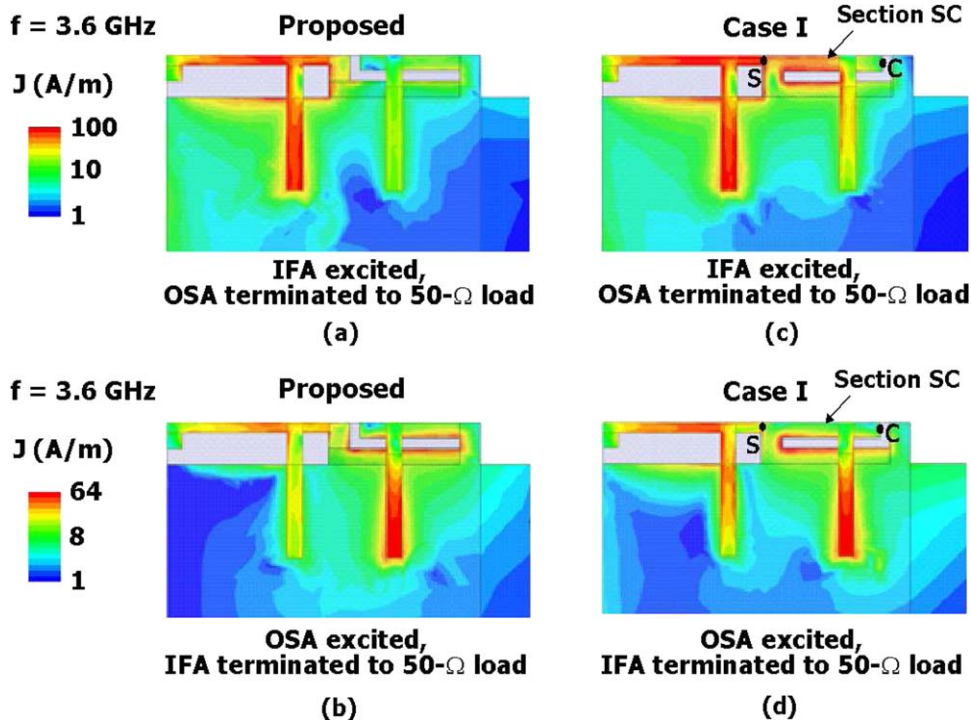


Figure 3 Simulated surface current distributions on the proposed design and Case I shown in Figure 2. (a) Proposed with IFA excited, (b) proposed with OSA excited, (c) Case I with IFA excited, and (d) Case I with OSA excited. [Color figure can be viewed in the online issue, which is available at wileyonlinelibrary.com]

Details of the proposed hybrid dual-antenna are described in the study, and its working principle is addressed. Results of the hybrid dual-antenna are compared with those obtained for the dual-antenna formed by two same IFAs or two same OSAs. The hybrid dual-antenna is also fabricated, and the experimental results are presented. In addition, the MIMO performance of the hybrid dual-antenna is discussed.

2. PROPOSED DAUL-ANTENNA

2.1. The Hybrid Dual-Antenna Structure

Figure 1 shows the hybrid dual-antenna formed by an IFA and an OSA for the 3.6-GHz LTE operation (3.4–3.8 GHz) in the tablet computer. The dual-antenna is mounted along and flushed to the left corner of the long edge of the device ground plane, which is selected to have dimensions of $150 \times 200 \text{ mm}^2$ in this study. The

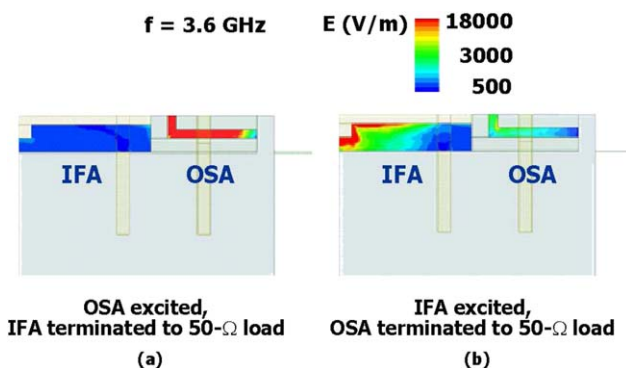


Figure 4 Simulated electric-field distributions inside the slot region of the OSA and the clearance region of the IFA for the proposed design. (a) OSA excited and (b) IFA excited. [Color figure can be viewed in the online issue, which is available at wileyonlinelibrary.com]

selected ground plane size fits for the 9.7-inch tablet computer. The dual-antenna has a planar structure and is printed on a 0.8-mm thick FR4 substrate of relative permittivity 4.4 and loss tangent 0.024. The dual-antenna occupies a size of $4 \times 30 \text{ mm}^2$, wherein the IFA is disposed in a clearance region of $4 \times 15.5 \text{ mm}^2$ and the OSA is

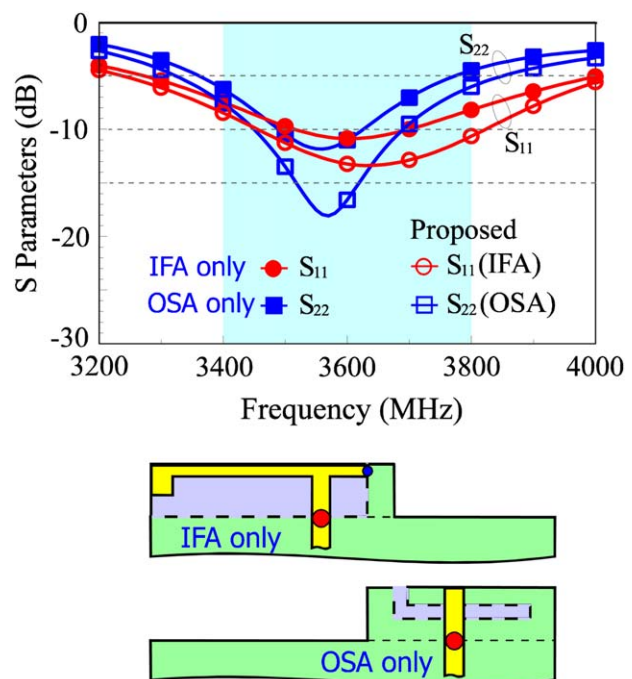


Figure 5 Simulated S parameters of the proposed dual-antenna, the case with the IFA only, and the case with the OSA only. [Color figure can be viewed in the online issue, which is available at wileyonlinelibrary.com]

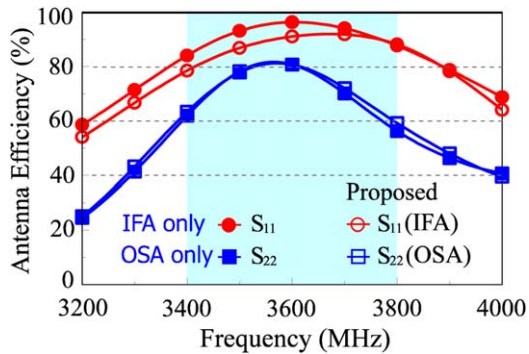


Figure 6 Simulated antenna efficiencies (mismatching loss included) of the proposed dual-antenna, the case with the IFA only, and the case with the OSA only. [Color figure can be viewed in the online issue, which is available at wileyonlinelibrary.com]

embedded in a metal pad of $4 \times 14.5 \text{ mm}^2$. The metal pad is electrically connected to the device ground plane.

The IFA and OSA are, respectively, excited at port 1 and port 2 through $50\text{-}\Omega$ microstrip feedlines. Their detailed dimensions are shown in the figure. The shorting strip of the IFA is connected to the metal pad through a via-hole at point S. The length of the IFA's radiating arm from point A to the open end thereof 18 mm, about 0.22 wavelength at 3.6 GHz. The OSA's slot length is 14 mm, about 0.17 wavelength at 3.6 GHz. Owing to the loading effects of the FR4 substrate, the required antenna's resonant length, especially for the OSA with a quarter-wavelength slot mode excitation [17,18], can be decreased. In this design, both IFA and OSA can generate a wide resonant mode to cover the desired 3.6-GHz LTE operation.

2.2. Working Principle and Antenna Performance

The working principle of the proposed hybrid dual-antenna is first studied. The open slot embedded in the metal pad is arranged to be extended away from the IFA. A comparison of the simulated S parameters of the proposed dual-antenna (open slot therein extending away from the IFA) and the case with the open slot therein extending toward the IFA (denoted as Case I in this study) is presented in Figure 2. The simulated results are obtained using the full-wave electromagnetic field simulator HFSS version 15 [19]. The dimensions of the open slot are the same for both cases. The IFA dimensions are also the same in both cases. With the selected antenna dimensions, the S_{11} (IFA) and S_{22} (OSA) of the proposed dual-antenna are less than -6 dB or 3:1 VSWR in the 3.4–3.8 GHz band. Similarly, the S_{11} and S_{22} of Case I are also less than -6 dB . That is, both cases are acceptable to cover the 3.6-GHz LTE band [16]. It is noted that the S_{21} of the proposed case is less than about -14 dB for the proposed case shown in Figure 2(a) and is better than that (less than about -9 dB) for Case I shown in Figure 2(b). The results suggest that the IFA-OSA arrangement in the proposed case can have better isolation between the two antennas.

It is also seen that the IFA's impedance matching (S_{11} curve) in Case I is enhanced, as compared with the corresponding S_{11} curve in the proposed design. Conversely, the OSA's impedance matching (S_{22} curve) is degraded for Case I, as compared with the proposed design. This is very likely because in Case I,

owing to the open slot extending away from the IFA, the Section SC [see the antenna structure inset in Fig. 2(b)] will function like an additional radiating arm for the IFA in the 3.6-GHz band. In this case, a π -shape IFA is formed [20], which leads to impedance matching enhancement for frequencies in the 3.6-GHz band. In addition, as the Section SC is excited by port 1 of the IFA, it is expected that the coupling between IFA and OSA in Case I will be enhanced. Also, with the undesired coupling through Section SC, the impedance matching of the OSA excited by port 2 is degraded [see the S_{22} curve in Fig. 2(a) vs. that in Fig. 2(b)]. This behavior can be seen more clearly in Figure 3, in which the simulated surface current distributions on the proposed design and Case I are presented. Figure 3(a) and 3(b) show the results for the IFA excitation or OSA excitation for the proposed design, while Figure 3(c) and 3(d) show the corresponding results for Case I. When the IFA is excited, strong surface current distributions on Section SC of the metal pad where the open slot is embedded are observed [see Fig. 3(c)]. When the OSA is excited, through the coupling of Section SC, the surface current distribution on the IFA is stronger for Case I than the proposed design [see Fig. 3(d) vs. Fig. 3(b)]. Based on the results shown in Figures 2 and 3, the hybrid dual-antenna with the proposed IFA-OSA arrangement is selected in this study.

To further confirm that the slot resonant mode is excited for the OSA, Figure 4 shows the simulated electric-field distributions inside the slot region of the OSA and the clearance region of the IFA for the proposed design. Results for the proposed design with the OSA-excitation case and the IFA-excitation case are presented.

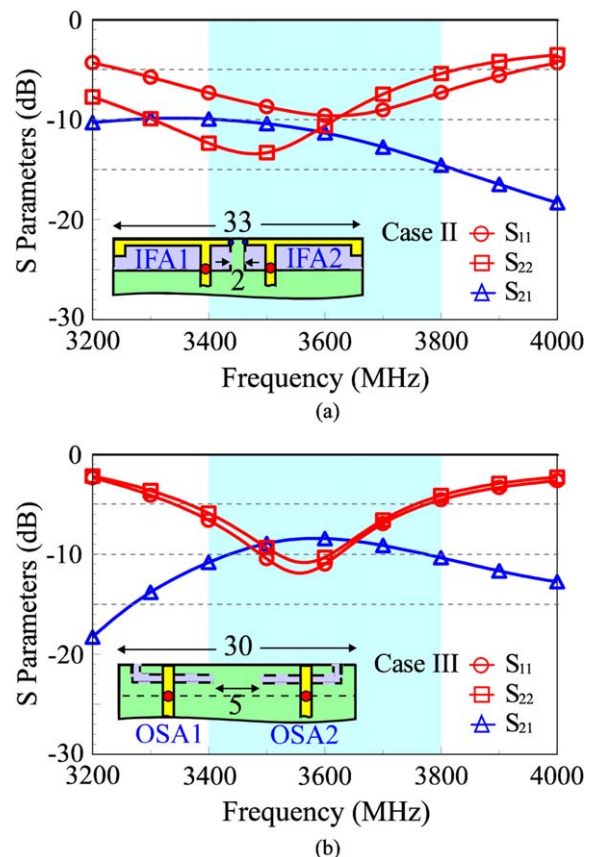


Figure 7 Simulated S parameters of (a) the case with two same IFAs (Case II) and (b) the case with two same OSAs (Case III). [Color figure can be viewed in the online issue, which is available at wileyonlinelibrary.com]

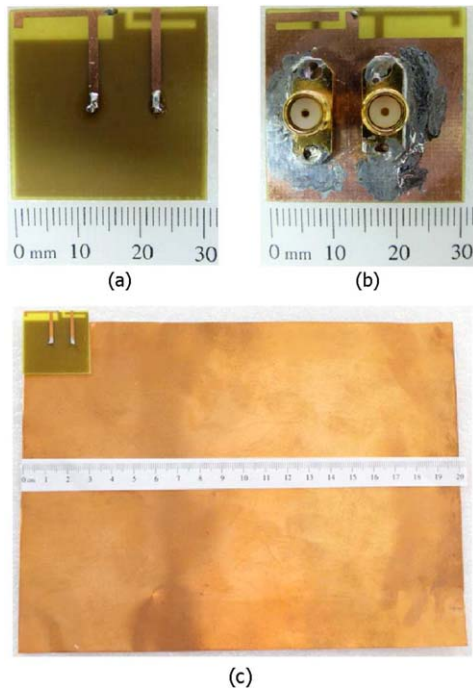


Figure 8 Photos of the fabricated dual-antenna. (a) front view, (b) back view, and (c) dual-antenna with the device ground plane. [Color figure can be viewed in the online issue, which is available at wileyonlinelibrary.com]

When the OSA is excited [see Fig. 4(a)], the electric-field distribution is about uniformly strong from the open end to across the feed-line and then becomes null at the closed end. This indicates that the open slot is strongly excited [21]. While for the IFA-excitation case [see Fig. 4(b)], the electric-field distribution along the two side edges of the clearance region is not symmetric, which is different from that in Figure 4(a). The electric-field distribution in the middle part of the clearance region is also much weaker, as compared with that in the slot region shown in Figure 4(a) for the OSA-excitation case. Due to some coupling from the IFA excitation, weak electric-field distribution in the open slot is also seen in Figure 4(b). Based on the different electric-field distributions observed in Figure 4(a) and 4(b), it can be confirmed that different resonant modes are excited for the OSA and IFA in the proposed design.

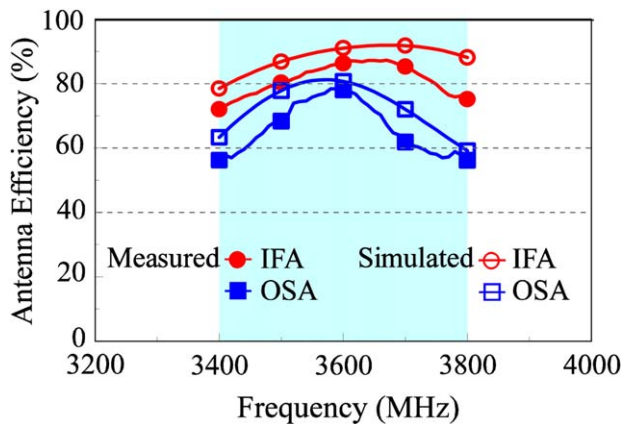


Figure 10 Measured and simulated antenna efficiencies of the fabricated dual-antenna. [Color figure can be viewed in the online issue, which is available at wileyonlinelibrary.com]

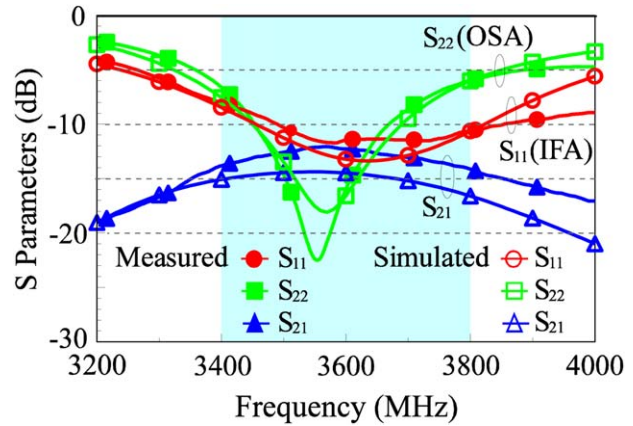


Figure 9 Measured and simulated S parameters of the fabricated dual-antenna. [Color figure can be viewed in the online issue, which is available at wileyonlinelibrary.com]

Effects of integrating the IFA and OSA into the proposed design are also studied. Figure 5 shows the simulated S parameters of the proposed dual-antenna, the case with the IFA only, and the case with the OSA only. The IFA shows improved impedance matching (see S_{11} curves) due to the OSA presence. Similar results are observed for the OSA (see S_{22} curves) with the presence of the IFA. This indicates that no degradation effects on the impedance matching are seen for the OSA presence to the IFA and the IFA presence to the OSA as well. This makes it convenient in the design of the proposed dual-antenna.

The simulated antenna efficiencies of the proposed dual-antenna, the case with the IFA only, and the case with the OSA only are shown in Figure 6. The antenna efficiency includes the mismatching loss. Although, there are some coupling between the two antennas (see the S_{21} curve in Fig. 2), the improved impedance matching seen in Figure 5 makes the antenna efficiency of the two antennas slightly decreased or about the same, as compared with the IFA-only and OSA-only cases.

2.3. Comparison with Two Same IFAs and Two Same OSAs

Results of the cases with two same IFAs and two same OSAs are also studied. Figure 7 shows the simulated S parameters of the case with two same IFAs (Case II) and the case with two same OSAs (Case III). For Case II, the two IFAs have same dimensions as in the proposed design, and they are placed back-to-back with their shorting strips connected to a small protruded ground. The total size of Case II is $4 \times 33 \text{ mm}^2$, which is slightly larger than that of the proposed design. With acceptable impedance matching in the 3.6-GHz band obtained for the two IFAs, the S_{21} is less than about -10 dB over the operating band [see Fig. 7(a)]. That is, Case II has worse isolation than the proposed design (less than -14 dB shown in Fig. 2).

For Case III shown in Figure 7(b), the two OSAs also have same dimensions as in the proposed design, and the distance between their open ends is selected to be 5 mm. In this case, Case III has a size of $4 \times 30 \text{ mm}^2$, same as the proposed design. The impedance matching of the two OSAs are both better than -6 dB , and the S_{21} is less than about -8 dB , which is also worse than the proposed design. The results shown in Figure 7 indicate that the proposed hybrid dual-antenna has better isolation than the cases with two same IFAs and two same OSAs.

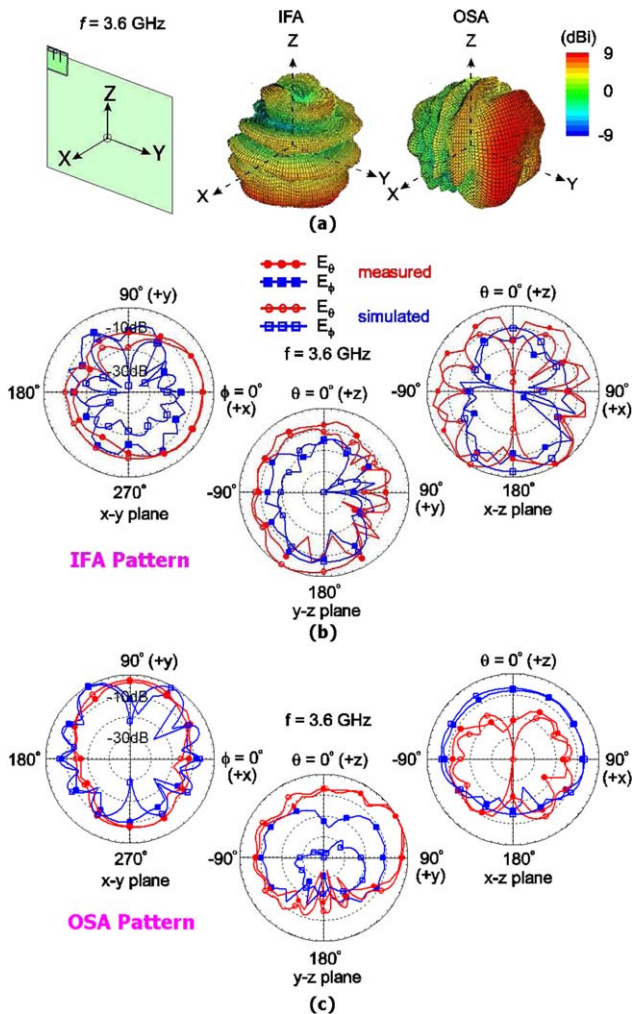


Figure 11 Measured and simulated radiation patterns of the fabricated dual-antenna. (a) Measured 3D radiation patterns, (b) 2D radiation patterns for the IFA, and (c) 2D radiation patterns for the OSA. [Color figure can be viewed in the online issue, which is available at wileyonlinelibrary.com]

3. EXPERIMENTAL RESULTS AND DISCUSSION

3.1. Experimental Results

Figure 8 shows the photos of the fabricated dual-antenna with the device ground plane cut from a 0.2-mm thick copper plate. The measured and simulated S parameters of the fabricated dual-antenna are shown in Figure 9. The measured S_{11} and S_{22} are similar to those of the simulated results. The measurement confirms that both the IFA and OSA can cover the 3.6-GHz band. The measured S_{21} also generally agrees with the simulated results and is less than about -12 dB over the operating band.

Figure 10 shows the measured and simulated antenna efficiencies of the fabricated dual-antenna. The antenna efficiencies were measured in a far-field anechoic chamber. The measured efficiencies of the IFA and OSA are, respectively, about 72–86 and 57–78%, which are acceptable for practical mobile communication applications [16]. It is observed that the measured efficiencies are slightly less than the simulated results. This may be related to the material loss of the FR4 substrate used in the experiment. In the simulation study, the loss tangent of the FR4 substrate is set to be 0.024. The used FR4 substrate in the 3.6-GHz band may have a larger loss tangent than that used in the simulation study.

Figure 11 shows the measured and simulated radiation patterns of the fabricated dual-antenna. The measured three-dimensional radiation patterns [see Fig. 11(a)] of the IFA and OSA are seen to be quite different or independent to each other. This behavior is largely owing to the different excitation mechanisms of the IFA and OSA and is advantageous to achieve a lower envelope correlation coefficient (ECC) for the MIMO operation [22]. The 2D radiation patterns at 3.6 GHz for the IFA and OSA are also shown in Figure 11(b) and 11(c). Radiation patterns in the three principal planes [x - y plane (azimuthal plane), y - z plane (elevation plane parallel to the device ground plane), and x - z plane (elevation plane orthogonal to the device ground plane)] are plotted. The radiation intensities in the three planes are normalized with respect to the same maximum intensity. The measured patterns are seen to generally agree with the simulated results. It is interesting to note that the radiation in the lower half-plane (see the y - z and x - z planes in the $-z$ direction) is weaker than that in the upper half-plane (see the y - z and x - z planes in the $+z$ direction) for the OSA. This indicates that the device ground plane mainly functions like a reflector for the OSA. Conversely, strong radiation in both the lower and upper half-planes of the elevation planes for the IFA is observed. This suggests that the device ground plane, although its dimensions are smaller than the operating wavelength at 3.6 GHz, still contributes to the radiation at 3.6 GHz for the IFA. This behavior may also lead to large differences seen in the 3D patterns for the IFA and OSA seen in Figure 11(a).

3.2. MIMO Performance

The ECC of the fabricated dual-antenna is studied with the aid of Figure 12. The calculated ECC from the measured 3D radiation patterns [22] is shown in the figure. The simulated ECC obtained from the HFSS version 15 [19] is also shown for comparison. For the ECC calculation, the indoor propagation environment is assumed, and the θ and ϕ polarized power functions of the incident wave are both set to $1/4\pi$ in all directions. From the obtained results, the simulated ECC is very small, close to 0. The ECC calculated from the measured radiation patterns is also small, less than 0.1, which is good for the MIMO operation [22].

Figure 13 shows the calculated MEG from the measured radiation patterns, and the simulated MEG obtained from the HFSS version 15 is also shown for comparison. The calculated and simulated MEGs show similar results. The differences between the calculated MEGs for the IFA and OSA are seen to be less than 2 dB, which is acceptable for practical applications [9].

Figure 14 shows the calculated channel capacities of the fabricated dual-antenna in a 2×2 MIMO system. For the capacity calculation, the condition of uncorrelated transmitting antennas and i.i.d. (independently, identically distributed) channels with Rayleigh fading environment is assumed. The obtained capacities are averaged over 10,000 Rayleigh fading realizations with a SNR (signal-to-noise) ratio of 20 dB for each frequency. The results show that the capacity for the proposed dual-antenna can reach about 9.8–10.6 bps/Hz, which is close to the upper limit of a 2×2 MIMO system with the two antennas thereof having perfect antenna efficiencies of 100% and a perfect ECC of 0. The obtained capacity is also much larger than the upper limit (5.75 bps/Hz) of a single-antenna (SISO, Single-input Single-output) with a perfect antenna efficiency of 100%. The results suggest that the proposed hybrid dual-antenna is promising for the MIMO application.

4. CONCLUSION

A hybrid dual-antenna formed by combining an IFA and an OSA into a compact structure for the 3.6-GHz LTE operation in the tablet computer has been proposed. The dual-antenna occupies a small

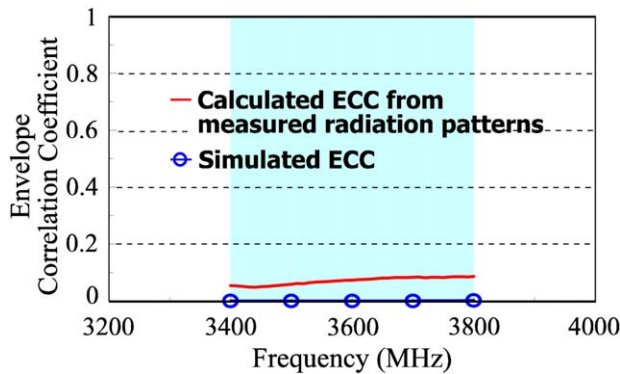


Figure 12 Calculated ECC from the measured radiation patterns and simulated ECC from the HFSS. [Color figure can be viewed in the online issue, which is available at wileyonlinelibrary.com]

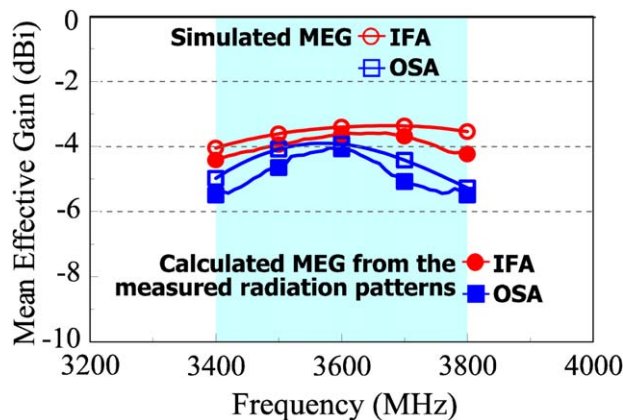


Figure 13 Calculated MEG from the measured radiation patterns and simulated MEG from the HFSS. [Color figure can be viewed in the online issue, which is available at wileyonlinelibrary.com]

planar size of $4 \times 30 \text{ mm}^2$, and acceptable isolation between the IFA and OSA has been obtained. The two antennas also show acceptable antenna efficiencies and the calculated ECCs from the measured radiation patterns are less than 0.1 over the operating band. The calculated capacities are also close to the upper limit of the 2×2 MIMO system. From the obtained results, the proposed hybrid dual-antenna is promising for the MIMO application.

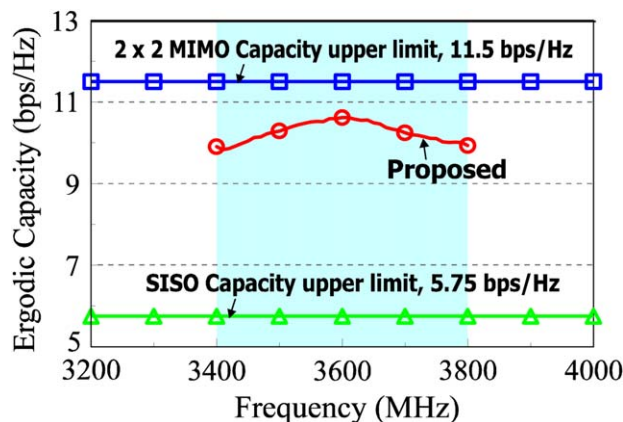


Figure 14 Calculated channel capacities of the fabricated dual-antenna in a 2×2 MIMO system. [Color figure can be viewed in the online issue, which is available at wileyonlinelibrary.com]

REFERENCES

1. X. Ling and R. Li, A novel dual-band MIMO antenna array with low mutual coupling for portable wireless devices, *IEEE Antennas Wireless Propag Lett* 10 (2011), 1039–1042.
2. S.W. Su, C.T. Lee, and F.S. Chang, Printed MIMO-antenna system using neutralization-line technique for wireless USB-dongle applications, *IEEE Trans Antennas Propag* 60 (2012), 456–463.
3. Y. Wang and Z. Du, A wideband printed dual-antenna system with a novel neutralization line for mobile terminals, *IEEE Antennas Wireless Propag Lett* 12 (2013), 1428–1431.
4. C.H. See, R.A. Abd-Alhameed, Z.Z. Abidin, N.J. McEwan, and P.S. Excell, Wideband printed MIMO/diversity monopole antenna for WiFi/WiMAX applications, *IEEE Trans Antennas Propag* 60 (2012), 2028–2035.
5. Y. Wang and Z. Du, A wideband printed dual-antenna with three neutralization lines for mobile terminals, *IEEE Trans Antennas Propag* 62 (2014), 1495–2000.
6. A. Cihangir, F. Ferrero, G. Jacquemod, P. Brachat, and C. Luxey, Neutralized coupling elements for MIMO operation in 4G mobile terminals, *IEEE Antennas Propag Lett* 13 (2014), 141–144.
7. K.L. Wong, T.W. Kang, and M.F. Tu, Internal mobile phone antenna array for LTE/WWAN and LTE MIMO operations, *Microwave Opt Technol Lett* 53 (2011), 1569–1573.
8. K.L. Wong, P.W. Lin, and H.J. Hsu, Decoupled WWAN/LTE antennas with an isolation ring strip embedded there between for smartphone application, *Microwave Opt Technol Lett* 55 (2013), 1470–1476.
9. Y.L. Ban, S. Yang, Z. Chen, and J.L.W. Li, Decoupled planar WWAN antenna with T-shaped protruded ground for smartphone applications, *IEEE Antennas Wireless Propag Lett* 13 (2014), 483–486.
10. T.W. Kang and K.L. Wong, Isolation improvement of 2.4/5.2/5.8 GHz WLAN internal laptop computer antennas using dual-band strip resonator as a wavetrap, *Microwave Opt Technol Lett* 52 (2010), 58–64.
11. S. Zhang, Z. Ying, J. Xiong, and S. He, Ultrawideband MIMO/diversity antennas with a three-like structure to enhance wideband isolation, *IEEE Antennas Wireless Propag Lett* 8 (2009), 1279–1282.
12. K.L. Wong, C.H. Chang, B. Chen, and S. Yang, Three-antenna MIMO system for WLAN operation in a PDA phone, *Microwave Opt Technol Lett* 48 (2006), 1238–1242.
13. M. Karaboikis, C. Soras, G. Tsachtsiris, and V. Makios, Compact dual-printed inverted-F antenna diversity systems for portable wireless devices, *IEEE Antennas Wireless Propag Lett* 3 (2004), 9–14.
14. J.J. Kim and K.H. Ahn, The high isolation dual-band inverted F antenna diversity system with the small N-section resonators on the ground plane, *Microwave Opt Technol Lett* 49 (2007), 731–734.
15. LTE Frequency Bands & Spectrum Allocations—a summary and tables of the LTE frequency band spectrum allocations for 3G & 4G LTE - TDD and FDD, Available at: <http://www.radio-electronics.com/>.
16. K.L. Wong and T.W. Weng, Small-size triple-wideband LTE/WWAN tablet device antenna, *IEEE Antennas Wireless Propag Lett* 12 (2013), 1516–1519.
17. C.I. Lin and K.L. Wong, Printed monopole slot antenna for internal multiband mobile phone antenna, *IEEE Trans Antennas Propag* 55 (2007), 3690–3697.
18. K.L. Wong and L.C. Lee, Multiband printed monopole slot antenna for WWAN operation in the laptop computer, *IEEE Trans Antennas Propag* 57 (2009), 324–330.
19. ANSYS HFSS, Ansoft Corp., Pittsburgh, PA, Available at: <http://www.ansys.com/products/hf/hfss/>.
20. S.W. Su, C.H. Wu, W.S. Chen, and K.L. Wong, Broadband printed π -shaped monopole antenna for WLAN operation, *Microwave Opt Technol Lett* 41 (2004), 269–270.
21. K.L. Wong and F.H. Chu, Internal planar WWAN laptop computer antenna using monopole slot elements, *Microwave Opt Technol Lett* 51 (2009), 1274–1279.
22. M.S. Sharawi, Printed multi-band MIMO antenna systems and their performance metrics, *IEEE Antennas Propag Mag* 55 (2013), 218–232.

© 2015 Wiley Periodicals, Inc.